Active telomere elongation by a subclass of cancer-associated POT1 mutations

Annika Martin,[1,6] Johannes Schabort,[1,6] Rebecca Bartke-Croughan,[1,6] Stella Tran,[1] Atul Preetham,[1] Robert Lu,[1] Richard Ho,[1] Jianpu Gao,[1] Shirin Jenkins,[1] John Boyle,[1] George E. Ghanim,[2] Milind Jagota,[3] Yun S. Song,[3,4] Hanqin Li,[1,5] and Dirk Hockemeyer[1,5]

[1]Department of Molecular and Cell Biology, University of California, Berkeley, Berkeley, California 94720, USA; [2]MRC Laboratory of Molecular Biology; Cambridge CB2 0QH, United Kingdom; [3]Computer Science Division, University of California, Berkeley, Berkeley, California 94720, USA; [4]Department of Statistics, University of California, Berkeley, Berkeley, California 94720, USA; [5]Innovative Genomics Institute, University of California, Berkeley, Berkeley, California 94720, USA

Mutations in the shelterin protein POT1 are associated with diverse cancers and thought to drive carcinogenesis by impairing POT1's suppression of aberrant telomere elongation. To classify clinical variants of uncertain significance (VUSs) and identify cancer-driving loss-of-function mutations, we developed a locally haploid human stem cell system to evaluate >1900 POT1 mutations, including >600 VUSs. Unexpectedly, many validated familial cancer-associated POT1 (caPOT1) mutations are haplosufficient for cellular viability, indicating that some pathogenic alleles do not act through a loss-of-function mechanism. Instead, POT1's DNA damage response suppression and telomere length control are genetically separable. ATR inhibition enables isolation of frameshift mutants, demonstrating that the only essential function of POT1 is to repress ATR. Furthermore, comparison of caPOT1 and frameshift alleles reveals a class of caPOT1 mutations that elongate telomeres more rapidly than full loss-of-function alleles. This telomere length-promoting activity is independent from POT1's role in overhang sequestration and fill-in synthesis.

[*Keywords*: POT1; cancer; deep scanning mutagenesis; pluripotent stem cells; telomerase; telomere]

Supplemental material is available for this article.

Received November 25, 2024; revised version accepted January 27, 2025.

Mutations in POT1 have been identified in multiple cancer types, with an overall prevalence of up to 3% (Calvete et al. 2017; Shen et al. 2020; Wu et al. 2020; DeBoy et al. 2023). These cancer-associated POT1 (caPOT1) mutations are missense, splicing, or nonsense mutations that can be found throughout the POT1 gene and are almost exclusively heterozygous. Although a small subset of these POT1 mutations has been linked to familial cancer predisposition syndromes (Robles-Espinoza et al. 2014; Shi et al. 2014; Bainbridge et al. 2015; Chubb et al. 2016; Speedy et al. 2016; Wilson et al. 2017; McMaster et al. 2018; Li et al. 2022; Goldstein et al. 2023), the vast majority, >900 mutations on ClinVar, are found in sporadic cancers and have been annotated as variants of uncertain significance (VUSs). Therefore, a key challenge in understanding POT1's role in carcinogenesis is delineating which mutations are pathogenic and by which mechanism these mutations drive the disease. This challenge is complex, especially because POT1 plays key roles in multiple telomeric processes: protecting the telomeric overhang from aberrant DNA damage response (DDR) activation (Denchi and de Lange 2007), controlling telomere overhang generation and length (Hockemeyer et al. 2005, 2006; Palm et al. 2009; Glousker et al. 2020), limiting access of telomerase to the telomere (Loayza et al. 2004; Ye et al. 2004), and maintaining the C-rich telomeric strand through interaction with the CST complex (Takai et al. 2016; Cai et al. 2024).

POT1 VUS characterization is further complicated by the distribution of caPOT1 mutations throughout the gene rather than clustering into functionally defined regions. POT1 contains three oligonucleotide binding (OB) folds and a Holliday junction resolvase-like (HJRL) domain (de Lange 2018). While OB1 and OB2 mediate POT1's overhang binding, the split OB3 and HJRL domain are important for TPP1 heterodimerization (Fig. 1A). The occurrence of familial pathogenic truncating mutations in each of these POT1 domains, as well as variants that disrupt the starting methionine, indicates that caPOT1 mutations generate loss-of-function alleles and that POT1 may

[6]**These authors contributed equally to this work.**
Corresponding authors: hockemeyer@berkeley.edu, hanqinli@berkeley.edu

Article published online ahead of print. Article and publication date are online at http://www.genesdev.org/cgi/doi/10.1101/gad.352492.124. Freely available online through the *Genes & Development* Open Access option.

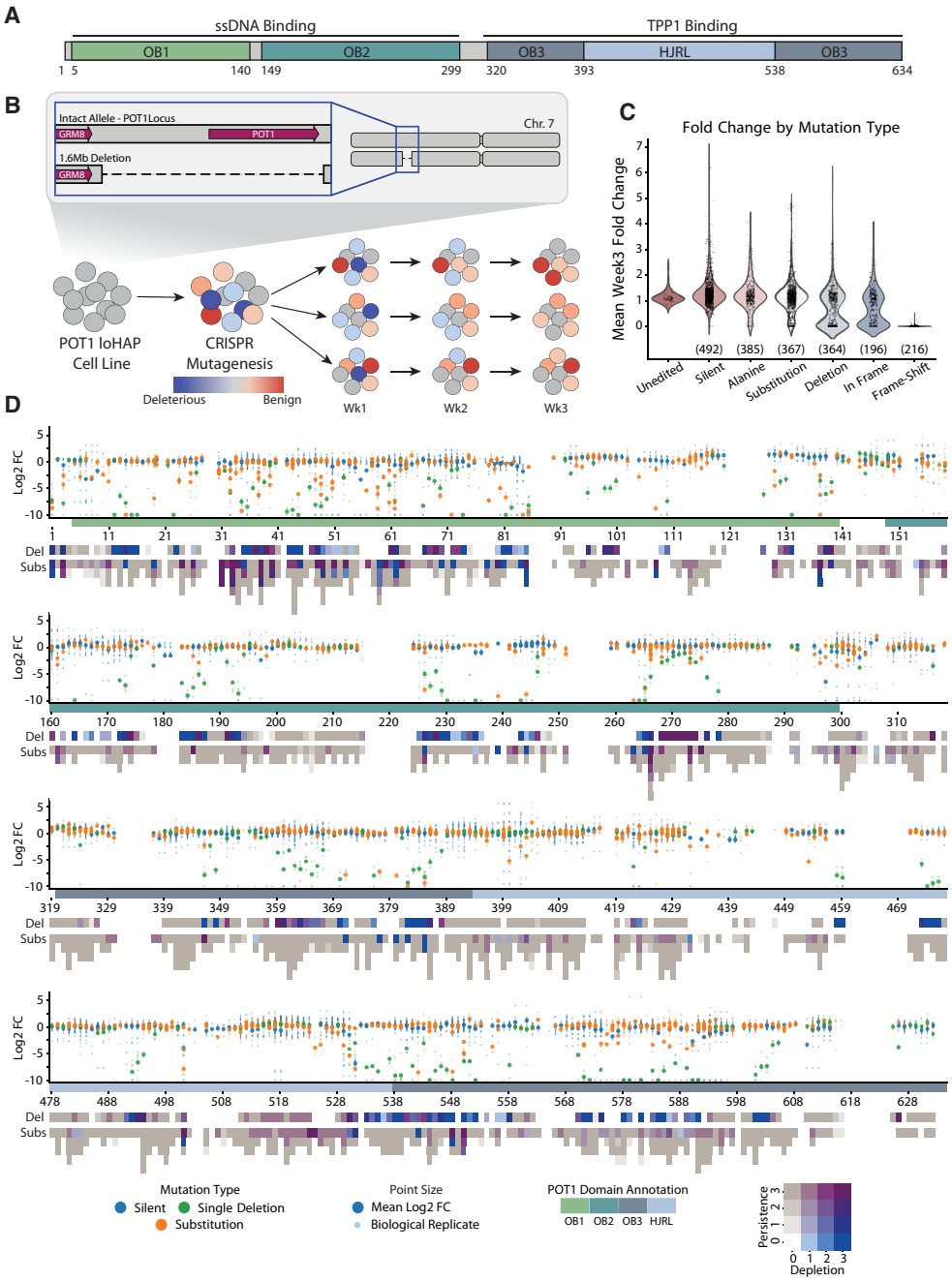

Figure 1. Deep scanning mutagenesis of POT1 reveals essential amino acids for cellular viability. (*A*) Schematic of POT1 protein domains. (*B*) Schematic of POT1 loHAP generation and screen timeline. Homology-directed repair (HDR)-mediated CRISPR/Cas9 mutagenesis of the remaining POT1 allele results in a spectrum of mutations with a direct genotype to phenotype correlation. Over 3 weeks of culture, the most deleterious alleles are depleted from the population. (*C*) Mean fold change in allele frequency across three biological replicates per allele between week 3 and week 1, stratified by mutation type: unedited, silent mutations, alanine substitutions, other substitutions (including clinical variants), precise single-codon deletions, other in-frame nonhomologous end-joining (NHEJ) events, and frameshift NHEJ events. (*D*) Summary dot plot of the week 3 $\log_2$ fold change for all silent mutations, substitutions, and single-codon deletions generated within the screen. Large dots indicate mean values at a given amino acid position, and smaller dots show individual biological replicates. The silent mutation mean for a given position is represented by the mean of all silent alleles carrying a codon change at that position, as silent alleles may contain codon changes at multiple positions. *Below* the dot plot is a domain map showing the location of the Holliday junction resolvase-like (HJRL) domain and OB folds. *Below* the domain map, persistence/depletion scores (see "Data Analysis—Allele Classification" in the Materials and Methods) for single-codon deletions (Del) and substitutions (Subs) are shown for each amino acid position. Blue (3,0) and taupe (0,3) indicate that all three biological replicates showed more allele depletion than synonymous mutations occurring at similar frequencies or less allele depletion than frameshift mutations, respectively. Purple (3,3) indicates hypomorphic alleles that persisted relative to frameshift mutations but were depleted relative to synonymous mutations. Gradations between these colors indicate differential behavior of biological replicates. White (0,0) indicates that the allele was not generated or that the allele could not be classified using these metrics. As multiple substitutions may occur at a single amino acid position, multiple squares at a given substitution position indicate unique amino acid substitutions. All screen results are shown in Supplemental Table S1.

function as a haploinsufficient tumor suppressor gene (Ramsay et al. 2013; Robles-Espinoza et al. 2014; Bainbridge et al. 2015; Calvete et al. 2015; Chubb et al. 2016). To efficiently annotate loss-of-function and hypomorphic POT1 variants, we performed deep scanning mutagenesis and detailed functional analysis to evaluate the effects of single amino acid deletions, alanine substitutions, and >600 POT1 VUSs. As caPOT1 mutations can be inherited or occur early in tumor progression prior to DNA damage checkpoint inactivation (Ramsay et al. 2013; Calvete et al. 2015), the functional annotation of POT1 variants requires a primary cell system with intact DDR and telomere maintenance pathways. Therefore, to mimic this primary, untransformed cell state while enabling direct genotype to phenotype characterization, we used a recently described system of locally haploid (loHAP) human embryonic stem cells (hESCs) to perform our mutagenesis screen and follow-up experiments (Li et al. 2024). The isolation and characterization of key dissociation-of-function mutations, along with a comparison with frameshift clones, identify a class of cancer-associated POT1 mutations that actively promote telomere elongation compared with full loss-of-function mutations.

Results

Deep scanning mutagenesis of POT1

POT1 loHAP cells were generated from diploid hESCs via 1.6 Mb excision of one allele, including upstream regulatory regions, using CRISPR/Cas9 (Fig. 1B). Successful loHAP generation was determined via junction sequencing, and clonality was confirmed by next-generation sequencing (NGS) of a single nucleotide polymorphism (SNP) on the remaining allele (Supplemental Fig. S1A). Mutations were introduced and allele frequency changes were evaluated as previously described for the BRCA2 locus (Fig. 1B; Li et al. 2024). As expected for an essential gene, frameshift mutations were strongly depleted in loHAPs within 3 weeks of editing compared with the diploid parental cells, whereas the allele frequency of unedited and synonymous alleles proportionally increased (Supplemental Fig. S1B,C).

Using single-stranded oligonucleotide pools as homology-directed repair (HDR) templates (Supplemental Fig. S1D,E), we evaluated mutations at 535 of 634 amino acid positions within POT1 (84.4%), including 385 alanine substitutions (63.0%; POT1 naturally contains 23 alanine residues), 364 single-codon deletions (57.4%), and 624 ClinVar VUSs and familial cancer mutations (Robles-Espinoza et al. 2014; Shi et al. 2014; Bainbridge et al. 2015; Chubb et al. 2016; Speedy et al. 2016; Calvete et al. 2017; Wilson et al. 2017; McMaster et al. 2018; Shen et al. 2020; Li et al. 2022) at 367 unique positions, with synonymous mutations at 492 unique positions (79.8%; 18 residues have no possible synonymous mutations) to act as controls. Allele depletion was evaluated by the $\log_2$ fold change of three independent biological replicates from week 1 to week 3 compared with synonymous and frameshift alleles (Fig. 1D; Supplemental Table S1). To aid in visualization, alleles were also assigned a persistence/depletion score based on the behavior of individual biological replicates relative to synonymous and frameshift mutations (see the Materials and Methods; Supplemental Fig. S1F). In general, alanine substitutions were more tolerated than single-codon deletions, though among all mutations surveyed, allele depletion was strongest at the N terminus of OB1 (amino acids 1–85) and the C terminus of OB3 (amino acids 538–634) (Fig. 1D; Supplemental Table S1).

Many pathogenic caPOT1 mutations are haplosufficient for cellular viability

Alanine and deletion scanning—coupled with existing structures of POT1 and its interactions with TPP1 and telomeric DNA—allowed us to generate a detailed map of residues essential to POT1 function and/or structural stability (Lei et al. 2004; Rice et al. 2017; Jumper et al. 2021; Aramburu et al. 2022; Tesmer et al. 2023). Although depleted alanine substitutions are comparatively dispersed (Supplemental Fig. S2A), depleted deletions tend to cluster into contiguous stretches that correspond to secondary structural elements (Supplemental Fig. S2B). Overall, 54% of single deletions within α helices and 82% of deletions within β strands show significant depletion, compared with 34% of deletions in unstructured regions (based on JPRED4 structural classification from Drozdetskiy et al. 2015 using a minimum confidence threshold of 3). Among the residues that were depleted, our screen demonstrates that C382 and C385 are essential (Fig. 2A). As these cysteines are proposed to coordinate a zinc ion (Lei et al. 2004; Rice et al. 2017; Aramburu et al. 2022), mutations at these residues may cause misfolding of POT1's HJRL domain and OB3. Likewise, alanine substitutions of large hydrophobic amino acids in the core of OB1 and OB2 were strongly selected against, suggesting that alanine substitution abrogates essential hydrophobic interactions within the OB cores, likely compromising protein stability (Fig. 2B).

In contrast, several mutations of POT1 residues that directly interact with single-stranded telomeric DNA (Lei et al. 2004; Tesmer et al. 2023) are well tolerated (Fig. 2C). Alanine substitutions at ssDNA-interacting residues of OB1, including F62 (which directly stacks against base T1 of the telomeric repeat sequence) and K33 (which interacts with the phosphate backbone of the ssDNA) (Lei et al. 2004), do show robust depletion. However, substitution at Y36, a residue that also contacts the ssDNA backbone, is not depleted. Alanine substitutions of key amino acids in OB2 also do not significantly impair cell viability over the course of 3 weeks, including H245, H266, Y271, and R273, which make numerous interactions with single-stranded telomeric DNA (Fig. 2C; Supplemental Fig. S3A; Lei et al. 2004). Mutations in the recently described POT-hole (Tesmer et al. 2023) also persist (Supplemental Fig. S3B–D), including residues R80, H82, and R83, which form a positively charged pocket contacting the ssDNA–dsDNA junction (Tesmer et al. 2023). Although previous in vitro experiments showed that alanine substitutions at these positions reduce POT1 binding to the ssDNA–

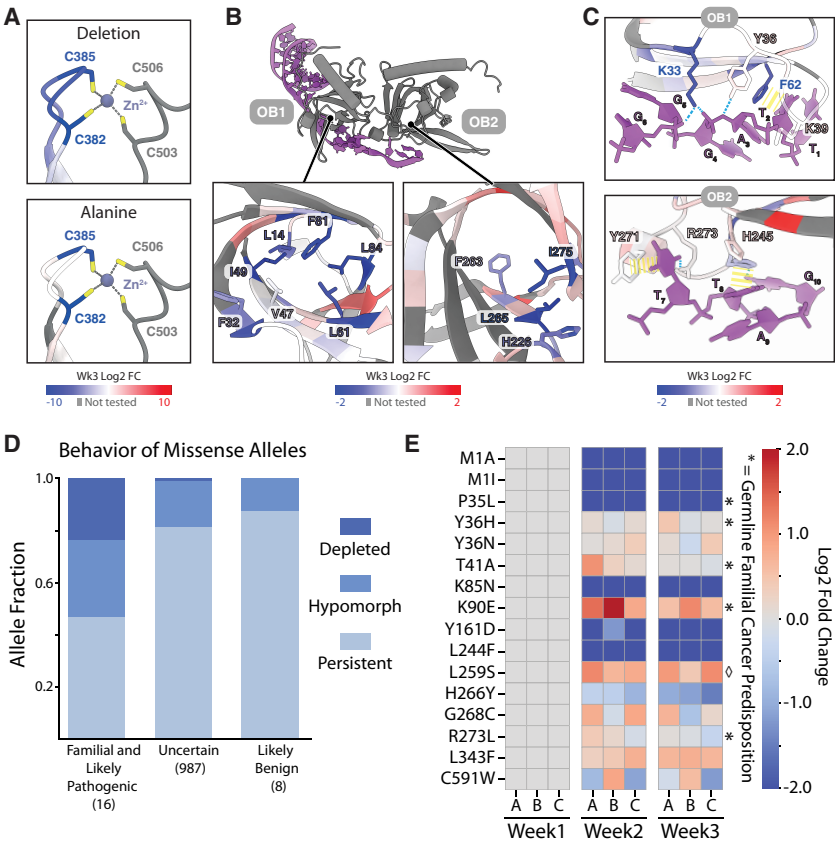

Figure 2. Many pathogenic caPOT1 mutations do not compromise cellular viability or abrogate essential POT1 functions. (*A*) Close view of zinc coordination by cysteines 382, 385, 503, and 506, colored by the week 3 $\log_2$ fold change in allele frequency of single-codon deletions (*top*) or alanine substitutions (*bottom*). The model was derived from PDB: 5UN7 (Rice et al. 2017). (*B*) POT1 (gray) interaction with telomeric DNA (magenta). The *inset* windows show hydrophobic residues at the center of OB1 (*left*) and OB2 (*right*) colored by $\log_2$ fold change in allele frequency of alanine substitutions. The model was derived from PDB: 8SH1 (Tesmer et al. 2023). (*C*) Closer view of the POT1–ssDNA interactions in *B* with the highlighted POT1 residues colored by $\log_2$ fold change in allele frequency of alanine substitutions. The model was derived from PDB: 1XJV (Lei et al. 2004). (*D*) Relative quantification of the proportion of alleles that are classified as persistent, hypomorphic, or depleted based on Wilcoxon rank sum comparison versus synonymous and frameshift mutations occurring at similar week 1 allele frequencies (see "Data Analysis–Allele Classification" in the Materials and Methods). Alleles are categorized as likely familial/likely pathogenic (based on ClinVar characterization, familial inheritance pattern, or disruption of the starting methionine), uncertain, or likely benign (based on ClinVar characterization). (*E*) Heat map showing $\log_2$ fold change of alleles classified as "likely pathogenic" in *D*, with three biological replicates shown across 3 weeks of allele sampling. (*) Germline familial cancer predisposition mutations, (◊) a variant identified in familial idiopathic pulmonary fibrosis (Kelich et al. 2022).

dsDNA junction (Tesmer et al. 2023), this interaction does not appear to be essential in our stem cell system. Interestingly, a small solvent-exposed acidic patch adjacent to the POT-hole formed by Y11 and D129 does show strong depletion, though its potential function is yet undefined (Supplemental Fig. S3D).

A similarly complex pattern arises with VUSs that impact POT1's interactions with TPP1. Alanine substitutions at residues F542, L574, and D577, which contact residues of TPP1's α helix 2 (Rice et al. 2017), are depleted over the course of 3 weeks (Supplemental Fig. S4A, left). However, interactions with TPP1's α helix 1, including W424 and L453, do not show a strong effect on viability (Supplemental Fig. S4A, right). A broader survey of amino acids contacting TPP1 confirms that only a small subset of mutations at the POT1–TPP1 interface impacts cellular viability (Supplemental Fig. S4B). In summary, only a fraction of caPOT1 mutations, including mutations in essential POT1 interaction domains, impaired cellular viability in our loHAP system over the course of 3 weeks. In fact, a substantial fraction of mutations that are likely pathogenic (based on ClinVar classification) or associated with familial cancer predisposition with a dominant inheritance pattern (Y36H, T41A, K90E, and R273L) did not impact cellular proliferation (Fig. 2D,E). One well-characterized familial mutation that falls into this class of mutations is R273L, which has been proposed to abrogate POT1's electrostatic binding with ssDNA by disrupting interaction with the telomeric dT7 nucleotide (Lei et al. 2004; Robles-Espinoza et al. 2014; Aramburu et al. 2022; Sekne et al. 2022). However, in our screen, both R273A and R273L were tolerated (Fig. 2C,E). Together, these findings demonstrate that cellular viability of hemizygous POT1 mutations does not faithfully predict pathogenicity or cancer predisposition.

Telomere elongation in caPOT1 alleles is uncoupled from telomere protection and DNA damage response signaling

Because validated, familial caPOT1 mutations include truncations, frameshift alleles, and mutations affecting the starting methionine (Ramsay et al. 2013; Robles-Espinoza et al. 2014; Bainbridge et al. 2015; Calvete et al. 2015; Chubb et al. 2016), caPOT1 mutations were considered loss-of-function alleles. We have previously demonstrated that heterozygous Y223C and Q623H caPOT1 mutations lead to telomere elongation without inducing a telomeric DDR (Kim et al. 2021). Conversely, overexpression of these alleles drives genomic instability (Chen et al. 2017; Gu et al. 2017). This has been interpreted as the ability of a wild-type POT1 allele to compensate for the caPOT1 allele in telomere end protection but

haploinsufficiency in telomere length regulation. Our finding that viability is not a reliable indicator of carcinogenic potential even in our hemizygous loHAP system complicates this interpretation and instead implies two additional possibilities: Telomere elongation may be directly linked to the degree of telomere deprotection, but telomeres elongate to pathogenic levels at a lower threshold of overhang exposure than would impair cellular viability. Alternatively, end protection and length regulation may be genetically independent, with hemizygously viable but pathogenic caPOT1 alleles promoting telomere elongation without affecting telomere protection.

To correlate DNA deprotection with telomere length, we first established the kinetics and frequency of telomere deprotection mutations by monitoring γH2AX telomere dysfunction-induced foci (TIFs) (Takai et al. 2003) following CRISPR/Cas9 mutagenesis. TIF burden surprisingly remained high for 3 weeks after mutagenesis despite the depletion of frameshift alleles (Supplemental Fig. S5A,B). In fact, a subset of TIF-positive cells (conservatively defined as a minimum of 10 TIFs per cell) was detectable in mutagenesis pools generated for every exon of POT1 beyond 3 weeks in culture (Supplemental Fig. S5C). Using a high-throughput genotyping and imaging analysis pipeline to directly annotate TIF-causing mutations by subpopulational sampling and Bayesian linear regression (Supplemental Fig. S5D,E), we estimate that >5% of all missense mutations present at week 3 in our mutagenesis pools generate TIFs.

Because TIF accumulation indicates overhang deprotection and increased accessibility of telomere ends, we predicted that persistent TIF-inducing alleles would result in telomere elongation. We therefore isolated clones from TIF-positive cell populations, including an allelic series of mutations surrounding the R273 familial cancer mutation; mutations around S322, which mediates POT1's interaction with CTC1 (Takai et al. 2016); and a clone with a single amino acid deletion of C349 proximal to POT1's interaction domain with TPP1. These clones show a broad range of persistent TIF phenotypes, demonstrating that the cells are surprisingly tolerant of partial overhang deprotection (Fig. 3A,B; Supplemental Fig. S5F–I). The ATR dependance of these persistent TIFs (Denchi and de Lange 2007) was confirmed via an intergenic knockout screen targeting DDR genes in T269Δ and C349Δ clones, in which ATR, RPA2, and TOPBP1 knockouts consistently lead to the greatest reduction in TIFs (Supplemental Fig. S5J,K). Knockout of RAD51 and RAD51AP1 also decreased TIFs, indicating a potential role of HDR machinery at the telomeres leading to checkpoint activation.

To establish that this persistent TIF phenotype reflects a graded response to partial telomere deprotection rather than artificial selection for clones incapable of responding to ATR signaling, we re-edited POT1 mutant clones at a secondary locus within the same POT1 allele (Fig. 3C). Although TIF-inducing mutations are well tolerated in loHAP cells or other TIF-negative cell lines, the same mutations show strong depletion in cells that already carry a TIF-inducing POT1 mutation (Fig. 3D; Supplemental Fig. S6A,B). This intragenic synthetic lethality indicates that additional POT1 mutations have compound effects on cellular viability and that distinct domains of POT1 similarly activate the ATR-mediated DDR, providing experimental evidence for previous predictions that POT1–TPP1 functions as a relay, adopting continuous conformations that differentially expose the telomeric overhang (Aramburu et al. 2022). It also suggests that there may be a cell-intrinsic threshold of tolerable ATR signaling that only triggers cell lethality if exceeded.

Surprisingly, TIF burden does not fully correlate with either telomere elongation or allele depletion in our screen. Any clones with a persistent DNA damage response at telomeres also have excessively elongated telomeres compared with clones harboring synonymous mutations (Fig. 3E; Supplemental Fig. S6C). Consistent with previous results (Takai et al. 2016; Cai et al. 2024), mutations affecting S322 also result in an overhang defect despite telomere elongation (Supplemental Fig. S6C). Similarly, many of the strongest TIF responses, including T269Δ and Y271Δ, result in moderate allele depletion (Fig. 3F). However, other DDR-activating mutations, including R273A, are completely neutral toward cell survival.

Furthermore, a small subset of POT1 mutations, including G268A (Fig. 3B,E) and M144A (Supplemental Fig. S6D, E), does not show a significant TIF phenotype and has no effect on cellular viability while still triggering dramatic telomere elongation. These separation-of-function mutants indicate that POT1's telomere length control is uncoupled from its essential role in telomere end protection, challenging the hypothesis that the only mechanism by which POT1 regulates telomerase activity is through steric hindrance and overhang sequestration. Either telomere extension occurs at a lower threshold of deprotection than can be detected by traditional TIF staining or POT1 plays a secondary, independent role in telomerase regulation that is yet undefined.

The only essential function of POT1 in hESCs is to repress ATR signaling

Because end protection and telomere length control can be genetically separated, the DDR and telomere elongation phenotypes in caPOT1 mutant cells may be co-occurring but independent effects of POT1 mutagenesis. Testing whether caPOT1 mutations elongate telomeres solely due to overhang deprotection or whether these alleles independently promote telomere extension requires direct comparison between caPOT1 alleles and full loss-of-function alleles. We hypothesized that dampening ATR signaling may allow deleterious alleles to persist in culture without reaching the DDR signaling threshold that triggers cellular lethality (Fig. 3G). Indeed, only ATR inhibition (ATRi) and not ATM inhibition (ATMi) increased the persistence of frameshift alleles (Fig. 3H) and enabled clonal isolation of frameshift mutants from all assayed POT1 protein domains, encompassing five different exons and spanning all three POT1 OB folds (Supplemental Table S2). These clones are stable in culture

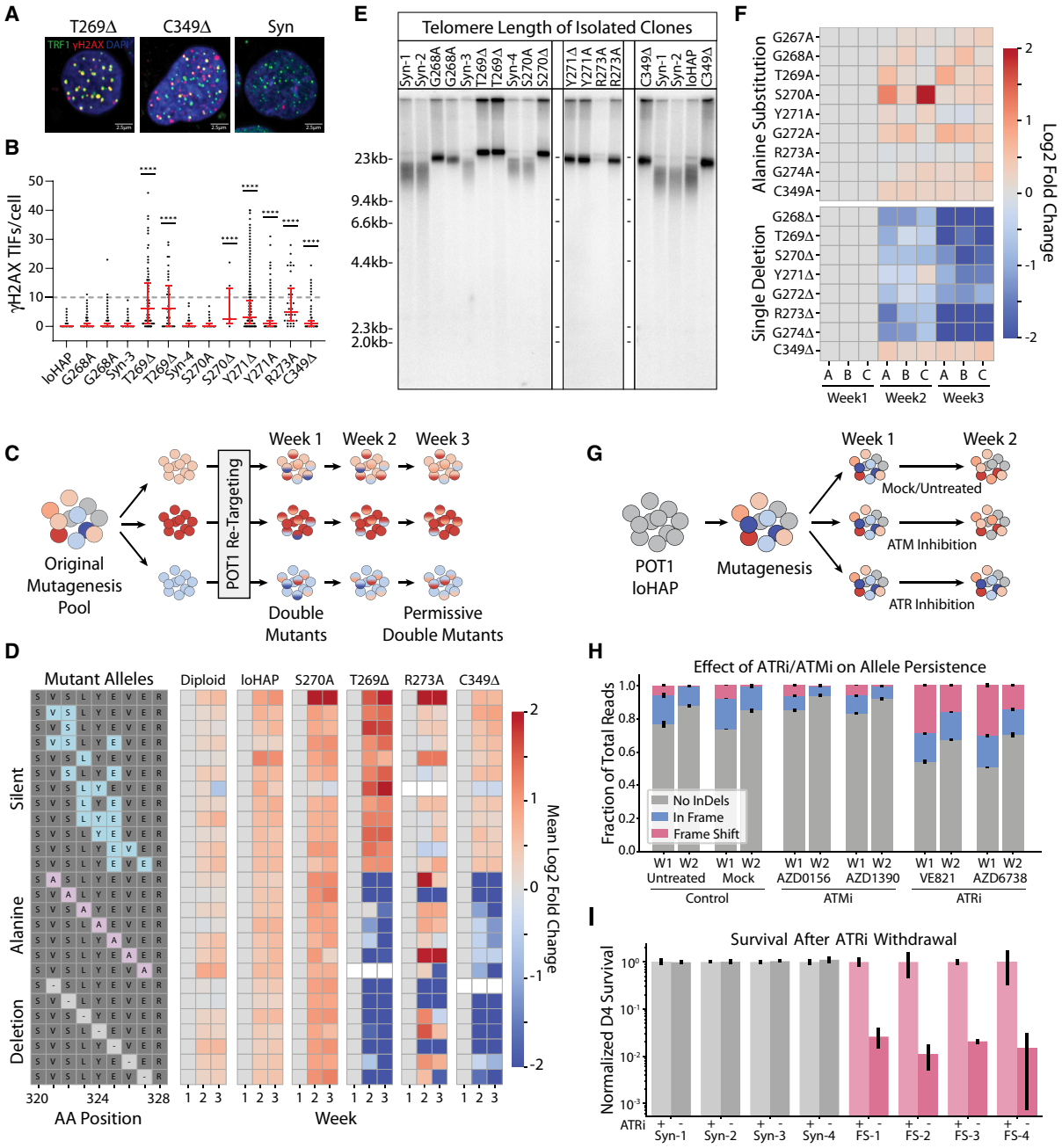

Figure 3. ATR inhibition stabilizes POT1 loss-of-function mutations. (*A*) Representative images for cells exhibiting the highest γH2AX TIF burdens in isolated T269Δ and C349Δ POT1 clones, characterized by the colocalization of TRF1 (green) and γH2AX (red) immunostaining signals. Scale bar, 2.5 µm. (*B*) Quantification of γH2AX TIFs per cell of clonally isolated POT1 mutants compared with unedited POT1 loHAPs. Duplicate genotypes indicate independently derived clones with the same mutation. Red error bars indicate median + interquartile range. Fisher's exact test with FDR correction for multiple comparisons of nuclei with ≥10 TIFs was done between each cell line and POT1 loHAP. (****) *P* value < 0.0001. (*C*) Schematic of intragenic synthetic lethality experiment: Clones isolated from the initial POT1 screen were retargeted to generate secondary mutations within the same POT1 allele that were then assayed over 3 weeks. (*D*) Results of retargeting experiment using sgRNA 73 and associated HDR templates. The heat map shows the mean $\log_2$ fold change of allele frequency of three biological replicates across 3 weeks of sampling for each indicated cell line (diploid wild type, loHAPs, S270A, T269Δ, R273A, and C349Δ). Alleles introduced by the POT1 retargeting are grouped by category: silent, alanine substitution, or single amino acid deletion. Alleles that were not detected in all three biological replicates in an indicated cell line are shown in white. (*E*) Telomere length analysis of clonally isolated POT1 mutant cell lines by Southern blot. Duplicate genotypes indicate independently derived clones with the same mutation. (*F*) Heat map showing mean $\log_2$ fold change of three biological replicates across 3 weeks of sampling for each indicated mutation. Alleles are grouped by mutation types. (*G*) Schematic of ATR/ATM inhibition screen. ATM inhibition (ATMi) or ATR inhibition (ATRi) was added immediately following sgRNA delivery. (*H*) Relative quantification of CRISPR/Cas9-mediated insertion and deletion alleles for 2 weeks after sgRNA delivery and drug treatment; three biological replicates are shown, with error bars representing the standard error of the mean. (*I*) Quantification of cell survival 4 days after ATRi withdrawal (–) compared with continued maintenance on ATRi (+) for four frameshift clones (pink) and four synonymous mutant clones (gray). Error bars show the standard error of the mean.

for >6 months provided ATRi is maintained. However, withdrawal of ATRi results in an ~100-fold reduction in cell viability within 4 days (Fig. 3I), indicating that persistence of POT1 loss-of-function clones under ATRi is not a result of clonal adaptation or ATR pathway silencing. Therefore, the only role of POT1 that is essential for cell survival is the suppression of ATR signaling.

Characterization of the DDR at telomeres in frameshift clones 48 h after ATRi withdrawal revealed that overall TIF burden significantly increased and EdU incorporation at telomeres can be detected outside of S phase (Fig. 4A,B; Supplemental Fig. S7A,B). These EdU foci correlate with a reduction in the number of telomere foci detected by TRF1 staining but an overall higher spot intensity (Fig. 4C,D), as well as accumulation of other DDR proteins including FANCD2 and RPA2 (pS33) (Fig. 4E–H; Supplemental Fig. S7A–K), consistent with previous reports that POT1 depletion activates HDR machinery at telomeres (Glousker et al. 2020). However, none of these phenotypes was detected under ATRi despite the fact that our ATRi is incomplete, as indicated by the presence of γH2AX and 53BP1 TIFs in frameshift clones under ATRi.

Conversely, telomeres do not incorporate EdU outside of S phase or recruit FANCD2 or RPA2 (pS33) in the T269Δ and C349Δ clones in standard media, whereas addition of ATRi abrogates the γH2AX TIF phenotype to background levels (Fig. 4A,B; Supplemental Fig. S7A–H). Therefore, TIFs in frameshift clones are both qualitatively and quantitatively different from those observed in cells harboring point mutations. This suggests that these clones represent a subactivated state of ATR signaling in which telomeres accumulate γH2AX and 53BP1 but fail to fully activate the downstream effectors of the ATR signaling cascade that would drive telomere recombination and cell lethality. It remains undetermined to what extent this lethality is due to direct ATR-dependent checkpoint signaling or the aberrant ATR-driven activation of HDR at the telomere (Buisson et al. 2017; Kim et al. 2018; Glousker et al. 2020). However, cell death occurs without the accumulation of overt telomeric defects, as detected by metaphase spreads (Supplemental Fig. S7L; Supplemental Table S3). We note that the frequency of metaphases detected in the frameshift clones after ATRi withdrawal was notably reduced, indicating that these cells may arrest or die prior to mitosis.

A novel class of caPOT1 mutations induces more rapid telomere elongation than POT1 frameshift mutations

Despite the ability of ATRi to repress DDR phenotypes in cells with point mutations, ATRi does not prevent telomere elongation. Derivation of R273L or C349Δ clones with or without ATRi consistently results in robust telomere elongation despite TIF frequency being reduced to near-background levels under ATRi (Fig. 5A,B; Supplemental Fig. S7M). Previous overexpression studies in cancer cells have implicated ATR in telomerase recruitment and telomere extension (Lee et al. 2015; Tong et al. 2015; Laprade et al. 2020). However, at the level of inhibition that we achieved in our cell system, we did not see any effect of ATRi on the degree of telomere hyperelongation in caPOT1 clones.

Surprisingly, simultaneously derived frameshift mutants at the same locus exhibit shorter telomeres than caPOT1 mutants 6 weeks after editing (Fig. 5B). This critically establishes that a subset of caPOT1 mutations has a stronger telomeric phenotype than full loss-of-function alleles, indicating that they must retain or gain a telomere length-promoting role. If both telomere elongation and DDR signaling were simply a function of overhang deprotection or if caPOT1 mutations merely compromised protein stability, then frameshift mutations should show the strongest degree of both telomeric phenotypes: deprotection and elongation. The rapid telomere elongation in the caPOT1 mutants compared with the frameshift mutants could be explained by three possibilities: First, POT1 frameshifts may compromise essential telomere maintenance or replication functions that are preserved in caPOT1 clones, thereby compromising total telomere elongation. Second, telomere elongation may be actively counteracted in frameshift clones, perhaps through nucleolytic degradation of unprotected telomeres. Third, caPOT1 alleles actively stimulate telomere elongation.

Loss of POT1 does not impair telomere replication or maintenance under ATRi

The simplest explanation for decreased telomere elongation in frameshift clones is that loss-of-function mutations result in an inability to properly replicate telomeres, because POT1 is thought to limit excessive 5′ resection and recruit the CST complex for fill-in synthesis of the lagging strand (Tesmer et al. 2023; Cai et al. 2024; Takai et al. 2024). CTC1 loss was previously shown to cause decreased cell viability as a function of gradual telomere loss and accumulation of single-stranded telomeric DNA (Feng et al. 2017). To confirm this phenotype in our hESCs, we engineered conditional $CTC1^{F/+}$ and $CTC1^{F/-}$ hESC lines such that induction of Cre recombination results in either $CTC1^{-/+}$ heterozygous or $CTC1^{-/-}$ null cells (Supplemental Fig. S8A). As expected, the loss of CTC1 led to a rapid increase in TIFs and an eventual loss of cell viability at ~24 days after loop-out of the conditional allele, concurrent with telomere shortening and overhang extension (Supplemental Fig. S8B–E).

Unlike the $CTC1^{-/-}$ null phenotype, POT1 frameshift clones under ATRi continuously elongate their telomeres over the course of several months (Fig. 5C). However, even after 13 weeks in culture, they do not recapitulate the uniform elongation and narrow window of telomere lengths of caPOT1 mutations at the same locus but instead show much more heterogeneous telomeres. This long-term telomere elongation in frameshift mutants is consistent across six independently derived clones compared with time-matched synonymous mutants (Fig. 5C; Supplemental Fig. S9A,B). Telomeres in POT1 frameshift mutants also do not show an overt overhang phenotype despite extended culture under ATRi, indicating that neither fill-in synthesis nor nucleolytic degradation likely

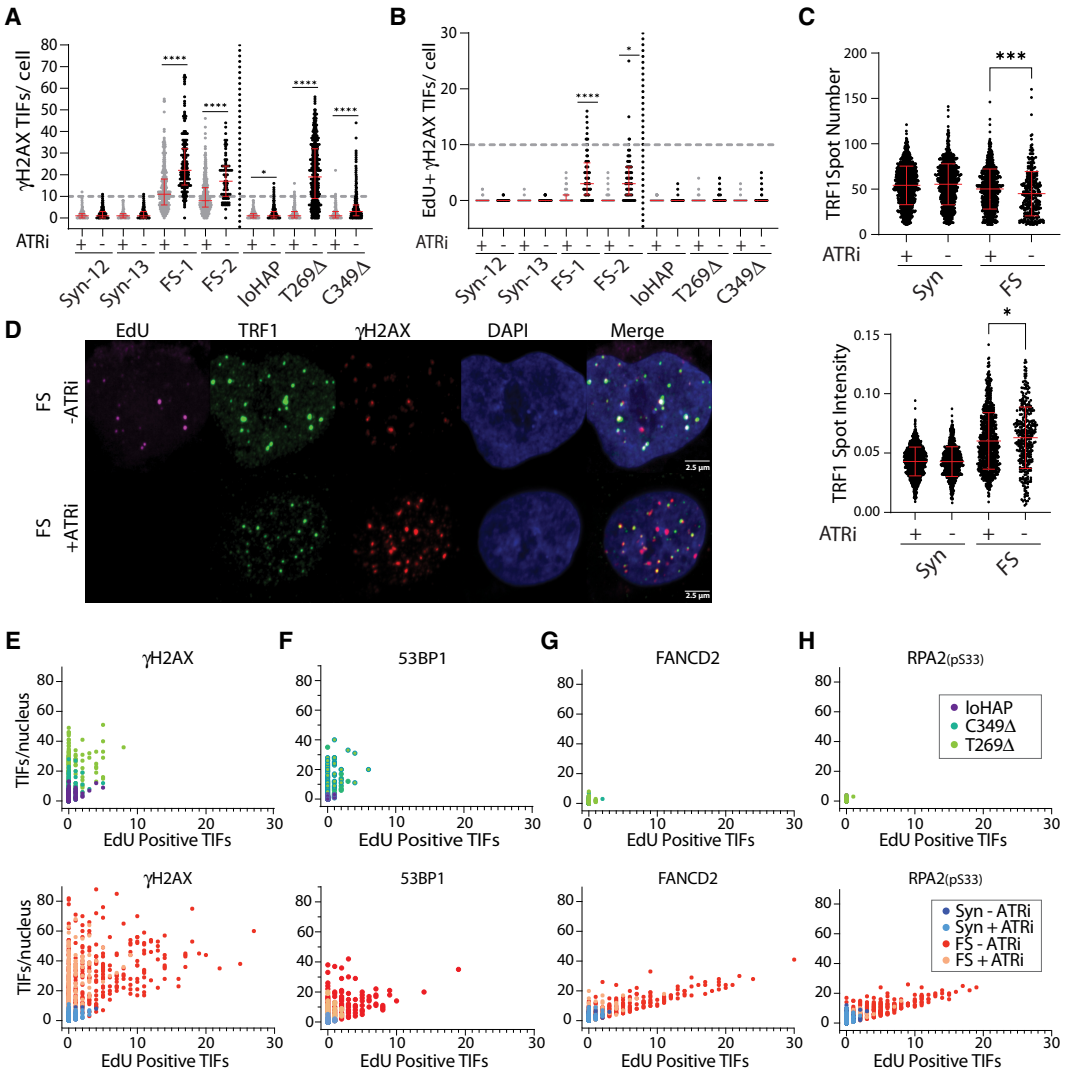

Figure 4. POT1 frameshift clones exhibit quantitatively and qualitatively different ATR-mediated TIFs than caPOT1 point mutation clones. (*A*) Quantification of γH2AX TIFs per cell under ATRi and 48 h after ATRi withdrawal for synonymous and frameshift clones (*left* of the dashed line) and with (+) or without (−) ATRi addition for 48 h for caPOT1 mutants (*right* of the dashed line). Red error bars indicate median + interquartile range. Fisher's exact test with FDR correction for multiple comparisons of nuclei with ≥10 TIFs was done between conditions with (+) and without (−) ATRi for each cell line. (*) *P* value ≤ 0.05, (****) *P* value ≤ 0.0001. (*B*) Quantification of γH2AX TIFs that colocalize with sites of EdU incorporation outside of S phase under ATRi and 48 h after ATRi withdrawal for synonymous and frameshift clones (*left* of the dashed line) and with (+) or without (−) ATRi addition for 48 h for caPOT1 mutants (*right* of the dashed line). Red error bars indicate median + interquartile range. Fisher's exact test with FDR correction for multiple comparisons of nuclei with ≥10 EdU-positive TIFs was done between frameshift (FS) and synonymous (Syn) cells and between mutant and POT1 loHAP cells. (*) *P* value ≤ 0.05, (****) *P* value ≤ 0.0001. (*C*) TRF1 spot number and spot intensity plots. Data are representative of four synonymous (Syn-12 through Syn-15) and four frameshift (FS-1 through FS-4) clones with (+) and without (−) ATRi. One-way ANOVA using Bonferroni's multiple comparison test was used to indicate significance. (∗) *P*-value ≤ 0.05, (∗∗∗) *P*-value ≤ 0.001. Red error bars indicate means + SD. (*D*) Representative images of EdU incorporation outside of S phase and γH2AX TIF colocalization outside of S phase in POT1 frameshift cells with (+) and without (−) ATRi. Scale bar, 2.5 µm. (*E*) Frequency plots for sites of EdU-positive γH2AX TIFs (*X*-axis) versus total γH2AX TIFs per cell (*Y*-axis). The *top* panel shows the frequency of distribution in loHAP, C349Δ, and T269Δ POT1 mutant cells, and the *bottom* panel shows frameshift (FS-1 and FS-2 combined) and synonymous mutations (Syn-12 and Syn-13 combined) with and without ATRi. (*F*) Frequency plots as in *E* for the colocalization of EdU-positive 53BP1 TIFs versus total 53BP1 TIFs per cell. (*G*) Frequency plots as in *E* for the colocalization of EdU-positive FANCD2 TIFs versus total FANCD2 TIFs per cell. (*H*) Frequency plots as in *E* for the colocalization of EdU-positive RPA2 (pS33) TIFs versus total RPA2 (pS33) TIFs per cell.

explains the slower telomere elongation phenotype (Fig. 5D). Following 72 h of ATRi withdrawal in frameshift clones, overhang signal significantly increases (Supplemental Fig. S9C). However, telomeres remain remarkably stable throughout the ATRi withdrawal, with no catastrophic telomere shortening or overt telomeric defects

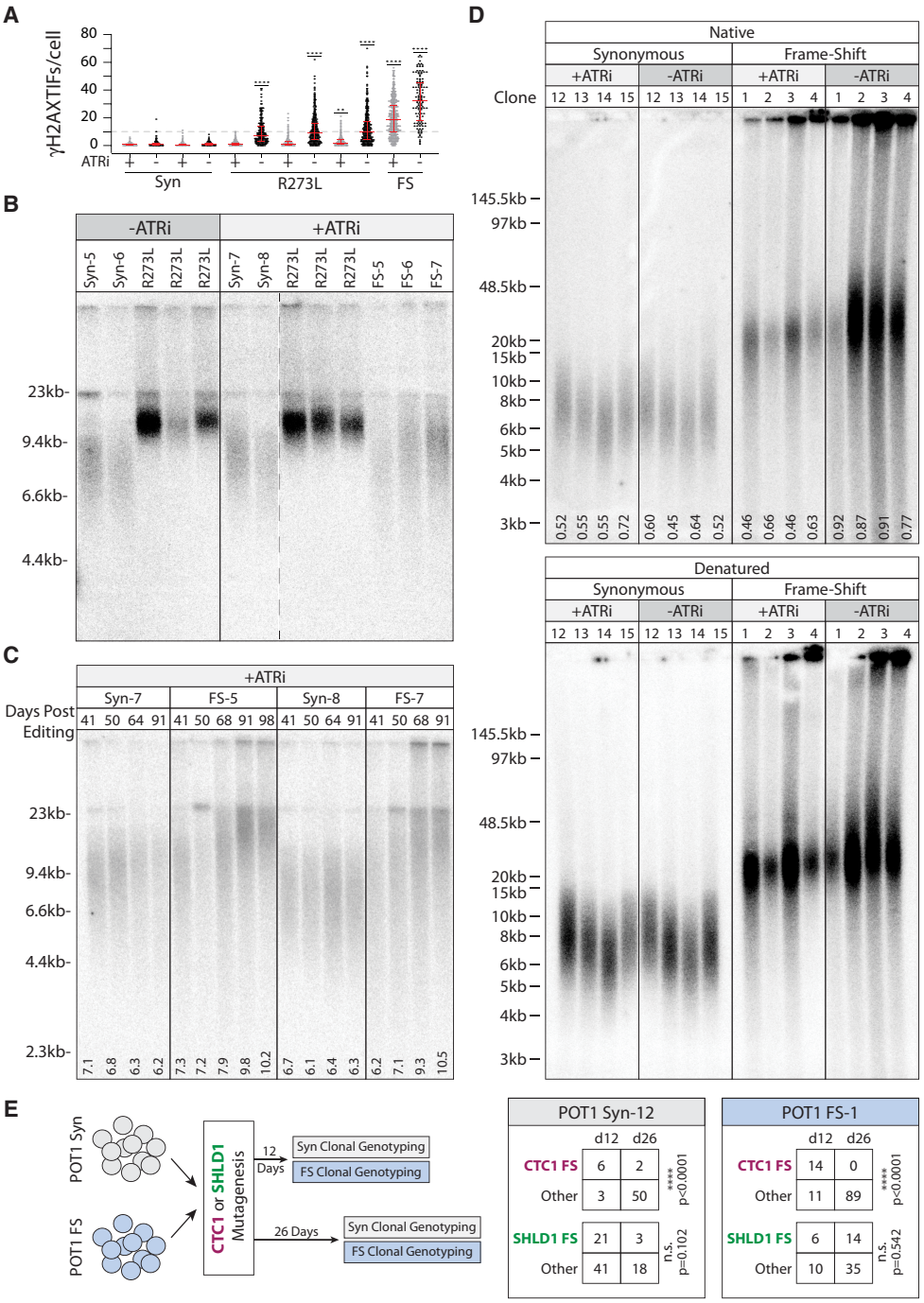

Figure 5. Telomere elongation driven by caPOT1 mutations is uncoupled from DDR signaling at telomeres, and POT1 is dispensable for telomere replication and maintenance under ATRi. (*A*) Quantification of γH2AX TIFs for mutants derived under ATRi. Withdrawal of ATRi is indicated *below* the *X*-axis. Red error bars indicate median + interquartile range. Fisher's exact test with FDR correction for multiple comparisons of nuclei with ≥10 TIFs was done relative to Syn cells without ATRi. (**) *P* value ≤ 0.01, (****) *P* value ≤ 0.0001. (*B*) Telomere length analysis of R273L, synonymous (Syn), and frameshift (FS) clones derived either under ATRi or without ATRi at 41 days after editing. Duplicate R273L genotypes indicate independently derived clones, whereas Syn and FS clones are labeled according to Supplemental Table S2. (*C*) Time-course telomere length analysis of two synonymous (Syn-7 and Syn-8) and two frameshift (FS-5 and FS-7) clones spanning days 41–98 after nucleofection. (*D*) Telomere length and overhang analysis of four synonymous (Syn-1 through Syn-4) and four frameshift (FS-1 through FS-4) clones 13 weeks after editing under ATRi and 72 h after ATRi withdrawal. Both native (*top*) and denaturing (*bottom*) conditions are shown. The telomere probe used was $(CCCTAA)_3$. Relative telomere overhang intensity (native intensity/denatured intensity) is quantified at the *bottom* of each lane in the native condition. Note that because intensity scales with telomere length as well as copy number, quantitative conclusions cannot be drawn between cell lines with differing telomere lengths. (*E*) CTC1 and SHLD1 targeting experiment in POT1 Syn-1 and POT1 FS-1 cells. POT1 Syn-1 and FS-1 cells were nucleofected as described in the Materials and Methods, and individual clones were genotyped at 12 and 26 days after nucleofection. "CTC1 FS" and "SHLD1 FS" refer to clones that carry homozygous or compound heterozygous frameshift mutations in CTC1 and SHLD1, respectively. "Other" refers to any clone that carries at least one unedited or in-frame-edited allele. Significance was determined by Fisher's exact test.

detectable prior to cell death (Supplemental Fig. S9B; Supplemental Table S3). Because recent in vitro studies show that priming for lagging strand DNA synthesis cannot occur at the telomeric overhang and requires CST to counteract lagging strand shortening (Takai et al. 2024), extension of the 3′ overhang via telomerase is insufficient to rescue shortening of the double-stranded portion of the telomere and prevent cell death. Therefore, fill-in synthesis must still be accomplished in our frameshift clones under ATRi despite loss of POT1, indicating that POT1 is not required for C-strand fill-in synthesis.

CTC1, however, remains essential in POT1 frameshift cells, as CTC1 knockouts in both POT1 frameshift and synonymous clones are viable at day 12 but show significantly reduced colony survival after 26 days in culture (Fig. 5E; Supplemental Fig. S9D), even though FS-1 cells start with much longer telomeres at the time of editing than our conditional CTC1 cell lines (Supplemental Figs. S8B, S9B). Because CST is also involved in DNA repair and because POT1 frameshift clones show DDR signaling at telomeres even under ATRi, we hypothesized that in POT1 frameshift clones, CST was recruited to telomeres via the DDR pathway instead of Shelterin-mediated telomere replication. To test this, we knocked out Shieldin complex subunit 1 (SHLD1), the Shieldin member that directly contacts both ssDNA and CTC1 (Boersma et al. 2015; Xu et al. 2015; Gupta et al. 2018; Mirman et al. 2018; Noordermeer et al. 2018). In contrast to CTC1, SHLD1 is dispensable for long-term proliferation in POT1 frameshift clones under ATRi (Fig. 5E). Therefore, CST-mediated C-strand fill-in synthesis is accomplished at telomeres independently of both POT1- and SHLD1-mediated recruitment.

We cannot entirely exclude the role of DDR factors in CST recruitment, as recent evidence suggests that CST may be recruited to dysfunctional telomeres independently of SHLD1 (Mirman et al. 2022). However, long-term maintenance of a normal telomeric overhang in the absence of POT1 indicates that the precise coordination of telomere end processing remains largely intact—an unlikely outcome of DNA repair pathways aberrantly acting at telomere ends. CTC1 can also interact with TPP1, and disruption of this interface results in telomere elongation (Wang et al. 2023). However, this TPP1–CST association appears to be mutually exclusive with TPP1–TIN2 tethering (Cai et al. 2024), and a precise method for CST recruitment and overhang maintenance in POT1-null cells remains to be resolved.

Discussion

The central findings of our deep scanning mutagenesis and variant characterization in POT1 are twofold: First, allele depletion of haploid caPOT1 mutations is not a reliable predictor of carcinogenic potential. Although we did identify many loss-of-function alleles that are not haplosufficient and would likely contribute to telomere elongation in a diploid setting, nearly half of the validated pathogenic mutations that we assayed show no significant depletion relative to synonymous alleles.

Second, because of our multiparallel analysis of >600 caPOT1 VUSs coupled with appropriate phenotypic characterization, we were able to identify a subclass of separation-of-function caPOT1 alleles that outperforms frameshift alleles in rapid telomere elongation. This establishes either that these alleles gain a de novo telomerase-activating function or that endogenous POT1 has a telomere length-promoting role that is lost in the frameshift mutants but preserved in the caPOT1 variants.

Because C-strand synthesis and telomere replication appear to be largely unchanged when cells without POT1 are cultured in ATRi, the extensive caPOT1-mediated elongation likely involves either protection of telomeric DNA from nucleolytic degradation or promotion of G-strand extension by telomerase. Both 5′ and 3′ nucleolytic degradation of telomere ends would result in telomeric overhang defects that were not detected in our clones despite long-term culture. Similarly, analysis of metaphase spreads indicates only a very slight increase in fragile telomeres and sister chromatid fusions, with very few signal-free ends. It also remains possible that POT1–CST interactions modulate the frequency or activity of C-strand synthesis because POT1 mutations at S322 in both this and previous studies show impaired fill-in synthesis (Takai et al. 2016; Cai et al. 2024). Therefore, inefficient or improper CST recruitment may cause a mild degree of overhang dysfunction that is not readily detected by native TRF and is sporadically corrected by association of CST with the telomere through other means. However, such a mild phenotype cannot explain the robust differences between caPOT1 and POT1 frameshift telomere elongation.

The overall lack of telomeric dysfunction in POT1 frameshift clones under ATRi leads us to favor another model: caPOT1 mutations may directly stimulate telomerase activity. This could either be through a true gain-of-function mechanism in which these caPOT1 alleles acquire de novo stimulatory effects or indicate that even wild-type POT1 plays an activating role in telomere elongation. Under this hypothesis, POT1's positive and negative effects on telomere length are carefully balanced in wild-type cells, whereas caPOT1 mutations represent a partial loss of function that relieves the inhibitory effects of POT1 while preserving its stimulatory capacity. The POT1–TPP1 heterodimer has been shown to increase telomerase repeat addition in vitro (Wang et al. 2007; Xin et al. 2007; Latrick and Cech 2010). Although the TPP1–TERT interaction is well characterized, the recently solved structure of telomerase bound to shelterin also suggests that POT1 directly contacts the TERT TEN domain (Ghanim et al. 2021; Sekne et al. 2022). Although this interaction has only been identified structurally, it highlights a key need for further genetic characterization of shelterin interactions with telomerase.

Alternatively, POT1's interaction with TPP1 may be required to properly recruit telomerase to the shortest telomeres. Although POT1 frameshift mutations under ATRi result in gradual telomere elongation, telomeres remain heterogeneous. At early time points, a subset of

telomeres appears to shorten, even relative to synonymous controls. Under normal telomere homeostasis, telomerase preferentially extends the shortest telomeres (Hemann et al. 2001; Teixeira et al. 2004). The persistence of short telomeres despite bulk elongation may therefore imply that loss of POT1 causes an overall increase in accessibility of telomere ends to telomerase but impairs targeted recruitment, perhaps by displacing or otherwise impacting TPP1. Thus, POT1 may also function as a telomerase-dependent positive regulator of telomere length, though the precise mechanisms remain unclear.

This suggests a model in which wild-type POT1 regulates telomere length homeostasis by controlling access of telomerase to the telomere end and repressing ATR-mediated DDR signaling (Fig. 6, top left). Loss of POT1 caused by frameshift mutations results in catastrophic DDR signaling, culminating in cell death. If ATR signaling is reduced to nonlethal levels via inhibition, telomerase has greater access to the 3′ telomeric overhang, resulting in telomere elongation. For this elongation, fill-in synthesis must still occur, though it remains possible that this process is mildly dysregulated without POT1 (Fig. 6, top right). However, some caPOT1 mutations reduce the ability of POT1 to repress telomerase activity and may in fact stimulate telomere elongation through an unknown mechanism while retaining the ability to regulate fill-in synthesis and maintain ATR-mediated DNA damage response signaling beneath a cellular threshold that would trigger telomeric recombination or cell death. Together, this results in rapid and dramatic telomere elongation relative to full loss-of-function alleles (Fig. 6, bottom).

Beyond the specific roles of POT1 mutations in telomere length regulation, the results of our deep scanning mutagenesis provide a cautionary note for the annotation of clinical variants of unknown significance. As tools for precise genome engineering continue to improve, parallel evaluation of thousands of disease-relevant single-nucleotide variants is becoming not only feasible but common practice (Li et al. 2024; Huang et al. 2025; Sahu et al. 2025). However, the persistence of carcinogenic variants within our POT1 screen emphatically demonstrates that variant annotation does not stop at dropout, even with cellularly essential genes. For many diseases, proper variant annotation will require looking beyond cellular survival.

Materials and methods

Human embryonic stem cell culture

Pluripotent stem cell research was approved under 2012-12-024 by the Stem Cell Research Oversight Committee at the University of California, Berkeley. WIBR3 hESCs (National Institutes of Health stem cell registry #0079) (Lengner et al. 2010) were cultured on 4.1×10^5 cm^{-2} of irradiated mouse embryonic fibroblasts (MEFs) in hPSC medium (Dulbecco's modified Eagle medium/nutrient mixture F-12 [DMEM/F12], 20% knockout serum replacement, 1× nonessential amino acids [NEAA], 1 mM glutamine, 1× penicillin/streptomycin, 0.1 mM β-mercaptoethanol, 4 ng/mL heat-stable basic fibroblast growth factor). The media was changed daily, and cells were passaged weekly with 1 mg/mL collagenase IV.

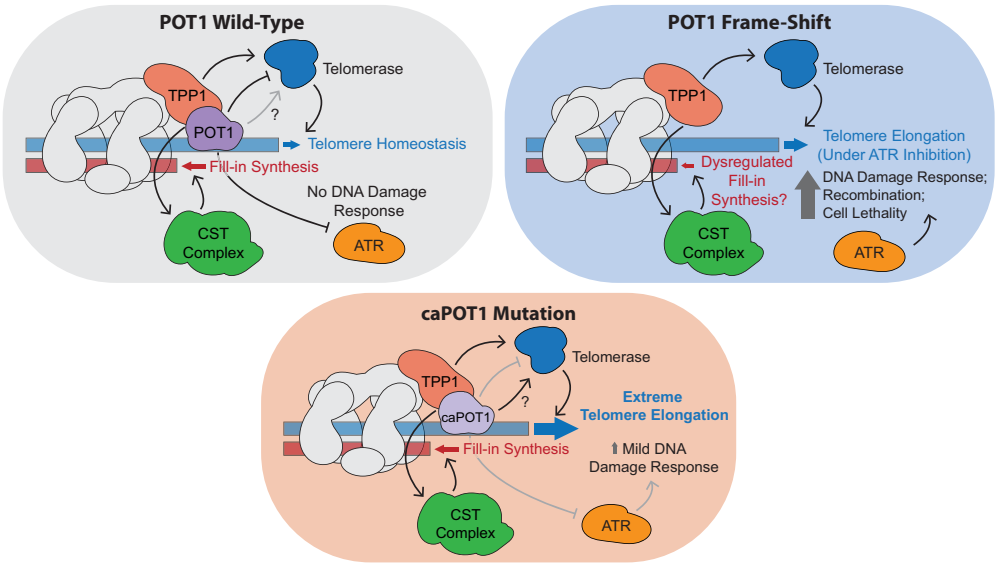

Figure 6. Model of POT1 interactions and telomere end homeostasis in a POT1 haploid setting. (*Top left*) Under wild-type conditions, POT1 represses ATR-mediated DDR, and telomere length homeostasis is maintained. (*Top right*) In POT1 frameshift mutations, ATR signaling is highly activated and results in cell death unless inhibited by ATRi; fill-in synthesis occurs but may be dysregulated, and telomeres elongate. (*Bottom*) In the case of caPOT1 mutations, ATR signaling may be partially activated, but DNA damage responses are mild; POT1 repression of telomerase activity is diminished, and fill-in synthesis is unaffected. A subclass of caPOT1 mutants retains or gains telomere length-promoting activity so telomeres elongate more dramatically and rapidly than frameshift alleles.

During screening, cells were cultured feeder-free using Matrigel-coated culture dishes and MEF-conditioned hSPC media (DMEM/F12, 20% knockout serum replacement, 1× (NEAA, 1 mM glutamine, 1× penicillin/streptomycin, 0.1 mM β-mercaptoethanol plated onto 4.1×10^5 cm^{-2} of irradiated MEFs for 24 h; harvested; and supplemented with 10 ng/mL heat-stable basic fibroblast growth factor). The media was changed every other day. Cells were single-cell-passaged weekly using Trypsin 0.25% EDTA, which was inactivated using 5% fetal bovine serum (FBS) added to the hPSC medium. The day before and the day after passage, the medium was supplemented with 10 µM Y27632 to increase cell survival.

Nucleofection of hESCs

hESCs cultured on MEFs were detached from feeder cells by treatment with 1 mg/mL collagenase IV for 20–30 min. Colonies were then suspended using hSPC wash media (DMEM/F12, 5% FBS, 1× penicillin/streptomycin) and then sedimented twice for 5 min at room temperature to remove MEF carryover. Following aspiration of the wash media and wash with phosphate-buffered saline (PBS), cells were dissociated to single cells by incubation with Accutase for 5 min at 37°C. Dissociated cells were washed with 10× volume of wash media, pelleted, resuspended in PBS, and counted.

Nucleofection was performed as described by Li et al. (2024). Briefly, 0.5 million–1 million hESCs were pelleted and resuspended in 20 µL of Lonza P3 nucleofection reagent, mixed with preassembled Cas9/sgRNA RNP with or without 100 pmol ssDNA oligo pool HDR donor templates, and nucleofected using program CA137 on Lonza nucleofector 4D.

Gene KO experiments were performed using multiguide gene knockout kit v2 (Synthego) targeting the specific genes of interest. Nucleofections were performed as described above. Cells were assayed for TIFs 7 days after nucleofection.

LoHAP generation

POT1 loHAPs were generated as described by Li et al. (2024). Briefly, sgRNAs were chosen based on specificity scores (Hsu et al. 2013; Haeussler et al. 2016) and location between 50 and 300 bp downstream from the transcriptional end sites of POT1 and GRM8. After nucleofection, cells are seeded onto 96 well plates at 1000 cells/well or 100 cells/well. After 12 days of outgrowth, cells were replica-plated, and the remaining cells were added to an equal volume of 2× PCR-compatible lysis buffer (100 mM KCl, 4 mM $MgCl_2$, 0.9% NP-40, 0.9% Tween-20, 500 µg/mL proteinase K, in 20 mM Tris at pH 8). The cell lysate was incubated overnight at 50°C and then heated for 10 min at 95°C to inactivate proteinase K. Cell clones were genotyped using Sanger sequencing of a junction-spanning PCR (PCR primers outside of the intended deletion) and NGS of a SNP located intronically between exons 15 and 16 (HG38 chromosome 7: 124837128 A/G). Primer sequences are listed in Supplemental Table S4. PCR was performed using either Titan or PrimeStarGXL polymerase using 2 µL of the lysate. Wells of interest with a single nucleotide remaining at a SNP were then further subcloned by low-density seeding or manual picking to ensure clonality.

Deep scanning mutagenesis

Mutagenesis was performed as described by Li et al. (2024), with minor adjustments. Targeted designer mutations were introduced with pools of 150–200 nt single-stranded oligonucleotide HDR templates centered at the CRISPR/Cas9 cut site. Oligo pools were purchased from Integrated DNA Technologies (IDT). HDR templates were designed with synonymous CRISPR/Cas9 blocking mutations to increase integration efficiency; when synonymous PAM-ablating mutations were not feasible, sgRNA-blocking mutations were introduced proximal to the cut site. All HDR templates contained a ≥2 nt change relative to the wild-type sequence to distinguish designer mutations from sequencing error.

Mutagenesis was performed by nucleofection into 1 million loHAP cells as described above, with the inclusion of 100 pmol of ssDNA oligo pool HDR donor templates. Immediately following nucleofection, cells were pooled based on sgRNA cut site location into pools that could be interrogated by a single sequencing amplicon (141 total sgRNAs divided into 16 pools) and then divided into three biological replicates derived from the same nucleofection event. Each biological replicate was cultured as described above and single-cell-passaged weekly at a ratio of 1:20. The remaining cells were split between two frozen cell stocks and two lysis tubes as described above in "LoHAP Generation."

Sequencing was performed by PCR amplification using Takara GXL polymerase, and the cell lysis equivalent of between 10,000 and 20,000 genomes were added per technical replicate. Between eight and 24 technical replicates were performed per biological replicate until the number of unique alleles detected was saturated. Amplicons were purified using SPRI bead purification at the University of California, Berkeley, DNA Sequencing Facility, i5/i7-barcoded, pooled, and run on 150 PE iSEQ for quality control before NextSeq or NovaSeq X deeper sequencing at the Center for Advanced Technology at University of California, San Francisco. All sequencing primers, HDR oligo templates, and sgRNA sequences are listed in Supplemental Tables 4–6, respectively.

Frameshift analysis

For single-sgRNA experiments, NGS fastq files were analyzed with CRISPResso2 (Clement et al. 2019) to merge reads, quality-filter, and separate alleles. Frameshift_analysis.txt outputs from CRISPResso2 were visualized into bar plots using the Python library Matplotlib.

Data analysis—allele classification

For pooled sgRNA mutagenesis experiments, demultiplexed NGS fastq files from each technical replicate

were initially analyzed using CRISPResso2 (Clement et al. 2019) to merge reads, quality-filter, and separate alleles per technical replicates. Allele frequency tables were then read into a custom Python script for further allele classification. First, alleles that showed full HDR (defined by complete integration of the HDR template) or partial HDR (defined by integration of the HDR template to one side of the predicted cut site) were identified. Next, cut site positions for all sgRNAs in the amplicon were used to define editing windows ±2 nt from any cut site position. Lesions not extending from these cut site positions were filtered out, and any single nucleotide substitutions not at cut sites and not generated by HDR were determined to be PCR error and corrected to wild type. Any alleles showing only a single nucleotide change (insertion, deletion, or substitution), alleles that were PCR-corrected to wild type, alleles showing multiple editing events, and alleles containing insertions were excluded from the analysis. The remaining alleles were translated in silico and collapsed based on the proposed protein changes.

Following allele classification, technical replicates were summed per amplicon, and only alleles with an overall allele frequency of $>1\times10^{-6}$ were retained. Alleles were then normalized to read depth to generate allele frequencies and then their respective week 1 samples to calculate fold change. To calculate $\log_2$ fold change and enable visualization of alleles that were completely depleted (and thus had a fold change of 0), 0.001 was added to all fold change values before applying the $\log_2$. Heat maps, dot plots, and other visualizations were generated using Matplotlib and Seaborn.

Alleles were then scored based on two metrics as follows:

Persistence/depletion scoring: To account for increased variance at lower allele frequencies, $\log_2$ fold change for each biological replicate was plotted against week 1 allele frequency, and the 95th or 5th percentile was calculated for frameshifts or synonymous mutants, respectively (as shown in Supplemental Fig. S1F), using a scanning window of 180 data points. Curves were fit to these percentile graphs using the scipy optimize.curve_fit module. Alleles were then classified based on these curves: For each biological replicate falling below the curve defined by the synonymous mutations, a depletion score of +1 was added, to a maximum of 3 (three biological replicates). Similarly, replicates above the frameshift curve were awarded a persistence score of +1, to a maximum of 3.

Statistical comparison: All alleles present in at least two biological replicates were statistically compared with the 180 synonymous and frameshift alleles closest to the same week 1 allele frequency. As frameshift alleles did not show a normal distribution, Wilcoxon rank sum was used to determine whether the allele fell significantly above the frameshift distribution and significantly below the synonymous distribution. Alleles that were not significantly depleted compared with the synonymous mutations were classified as persistent. Alleles that were not significantly enriched compared with the frameshift alleles were classified as depleted. Alleles significantly different from both were classified as hypomorphs.

Structural visualization

A Python script was used to map $\log_2$ fold change in allele frequency onto the PDB file B-factor column. Structural predictions were performed using AlphaFold2 through a local installation of Colabfold 1.2.0 (Mirdita et al. 2022), running MMseqs2 (Mirdita et al. 2019) for homology searches and AlphaFold2-Multimer (Evans et al. 2022) for the prediction. Models were visualized in ChimeraX (Goddard et al. 2018). PDB IDs are included in the figure legends.

TIF staining

Cells were plated on Matrigel-coated (Corning) phenoplate-96 imaging plates (Revvity) at a seeding density of ~20,000 cells/well 24 h prior to fixation with 4% paraformaldehyde for 10 min at room temperature. Following a wash in 1× PBS, cells were permeabilized in 0.1% Triton X-100 for 15 min at room temperature before an additional wash in 1× PBS and 15 min blocking in blocking buffer (3% BSA + 5% horse serum, 0.1% Tween-20 in PBS) at room temperature. Primary antibody (anti-TRF1 at 1/10,000, anti-TRF2 at 1/2000, anti-γH2AX at 1/2000, anti-53BP1 at 1/2000, anti-RPA32 s33 at 1/2000, and anti-FANCD2 at 1/2000) and secondary antibody (Alexa 488 antimouse IgG at 1/2000 and Alexa 546 antirabbit IgG at 1/1000) staining occurred consecutively for 1 h each at room temperature. All antibodies were diluted in blocking buffer as described above. Nuclei were stained with 0.05 µg/mL DAPI (Sigma-Aldrich) in PBS for 15 min at room temperature. Cells were washed twice in 1× PBS with 0.1% Tween-20 after each step of staining: primary, secondary, and DAPI.

For non-S-phase EdU incorporation assays, cells were treated with 10 µM R0-3306 (Sigma-Aldrich) 24 h prior to fixation, and 10 µM EdU was added 2 h prior to fixation. Staining was performed using the Click-iT Plus EdU Alexa fluor 647 imaging kit (Thermo Fisher Scientific) per the manufacturer's instructions prior to the commencement of additional immunofluorescent staining as outlined above.

All immunofluorescent images were captured using an Opera Phenix high-content imager with a 63× objective. Analysis was done using Harmony software (Revvity). *Z*-stacks were maximum image-projected, and TIFs were called based on >50% overlap of telomere and DDR spots.

Metaphase spreads/FISH

Cells were treated with colcemid at 100 ng/mL for 1.5 h, collected using trypsin, and incubated at 37°C in prewarmed 75 mM KCl. The cells were spun down, and the KCl was removed. Under agitation, cells were slowly resuspended in a fixative of 3:1 methanol:acetic acid and stored overnight at 4°C. Next, cells were spread dropwise onto cold, wet microscope slides and washed twice with 1

mL of 3:1 methanol:acetic acid solution. The slides were then air-dried and aged overnight at room temperature. Slides were washed with PBS and then dehydrated in an ethanol series. Each slide received 100 µL of hybridization mixture, was denatured for 5 min at 80°C, and then was hybridized overnight with Cy3 Tel-C probes (PNA Bio) and centromeric PNA probes (PNA Bio) at 4°C in a hybridization chamber. The next day, the slides were washed twice with 70% formamide, 10 mM Tris-HCl (pH 7.2), and 0.1% BSA solution and then twice with 0.1 M Tris-HCl (pH 7.2), 0.15 M NaCl, and 0.08% Tween, with DAPI (diluted 1:1000 from 5 mg/mL stock) added to the second wash. Coverslips were mounted with ProLong Gold antifade mountant (Thermo Fisher Scientific). All metaphase spreads were imaged on a Nikon Eclipse TE2000-E epifluorescent microscope equipped with an Andor Zyla sCMOS camera.

Alkaline phosphatase staining

After media was removed from hESCs grown on feeders, the plates were washed once in PBS and then treated with cold 4% PFA for 10 min at room temperature. The cells were then washed twice with PBS, and then 100 mM Tris-HCl (pH 9.5) was balanced in and left for 10 min at room temperature. One drop of each reagent from the Vector red alkaline phosphatase substrate kit I (Vector Laboratories) was added to 6 mL of 100 mM Tris-HCl and then added to the cells. Cells were developed in the dark for ~20 min at room temperature until the desired staining intensity was reached. Cells were washed once more and stored in PBS.

High-throughput imaging and a Bayesian regression model

Stabilized POT1 mutant pools (14 days after editing) were single-cell-dissociated and seeded onto 96 well plates using the Tecan Fluent liquid handler at a concentration of 30 cells/well based on an empirical 30% single-cell survival rate. The medium was changed every 3 days using Biotek EL406. At day 14, cells in each well were single-cell-dissociated and split evenly into three parts using Tecan Fluent. Part 1 was replated onto new MEF plates for maintenance, part 2 was mixed with 2× lysis buffer to generate gDNA lysis and then NGS-genotyped as described above, and part 3 was replated onto Matrigel-coated plates to generate the first batch of samples for imaging. The maintenance plates were then split the same way on day 21 to generate a second batch of samples for imaging. Both imaging samples were fixed 3 days after plating, immunostained for TIFs, and imaged as described above to measure the number of TIFs per cell. The TIF data from both imaging batches were combined, and the frequency of TIF^+ cells per well was calculated using TIF^+ criteria ≥10 TIF loci/cell. To reduce noise, wells that yielded <20 cells in imaging or failed in NGS genotyping were removed, and alleles that exhibited a frequency of <1% in all wells were binned into one low-frequency entry. The preprocessed allele frequency matrix and corresponding TIF^+ frequency array were then used as input for a Bayesian regression model with a predefined assumption that the coefficients of all alleles followed a β distribution ($a = 1$ and $b = 9$) because the majority of alleles, including all synonymous mutations, did not lead to TIF^+. Scripts for allele classification and Bayesian regression are available on GitHub.

Clonal isolation

Nucleofected cells were seeded onto 96 well plates at 10, 30, or 100 cells/well; alternatively, mutant pools were seeded at one, three, or 10 cells/well in hPSC medium with 10 µM Y27632. On day 12, plates were duplicated to generate gDNA lysis and then NGS-genotyped as described above. Wells that showed only one allele (>99% allele frequency) were expanded and genotype-confirmed to establish clonal cultures. To isolate frameshift mutations, the medium was supplemented with 1 µM AZD6738 ATRi.

Intragenic synthetic lethality

Each clone as well as the parental loHAP cells and diploid wild-type WIBR3 hESCs were nucleofected with a single sgRNA and accompanying ssDNA HDR oligopool as described above and then cultured and sampled according to the deep scanning mutagenesis protocol. Allele classification was performed as described previously.

ATM/ATR inhibition

POT1 loHAP cells were nucleofected as described above and then immediately split into three biological replicates per six conditions with hPSC media supplemented as follows: unsupplemented control, mock (0.1% DMSO), 1 µM AZD0156 ATMi, 1 µM AZD1390 ATMi, 10 µM VE821 ATRi, or 1 µM AZD6738 ATRi. Cells were cultured and sampled as described for 2 weeks before frameshift analysis was performed.

ATRi withdrawal

Synonymous and frameshift mutants maintained under ATRi were single-cell-dissociated using Accutase and seeded onto Matrigel-coated 96 well plates at 4000 cells/well with triplicates in hPSC medium with or without ATRi. Cells were fixed on day 5 using 4% PFA, stained with DAPI, and then imaged and counted on Celigo (Revvity).

Telomere length detection

Genomic DNA was prepared as described previously (Hockemeyer et al. 2005). Briefly, genomic DNA was digested with MboI, AluI, and RNase A overnight at 37°C. The resulting DNA was normalized, and 2 µg of digested DNA was resolved by standard gel electrophoresis either on a 0.75% agarose (Seakem ME agarose, Lonza) gel or on a 1% pulse-field gel at 6 V/cm in 0.5× TBE for 12 h

with an initial switch time of 1 sec and a final switch time of 6 sec using the CHEF DRIII pulse-field apparatus (Bio-Rad). Subsequently, gels were stained with ethidium bromide to confirm equal loading, dried under vacuum for 2 h at 50°C, denatured in 0.5 M NaOH and 1.5 M NaCl for 30 min at 25°C with shaking, and neutralized with 1 M Tris (pH 6.0) and 2.5 M NaCl twice for 15 min at 25°C with shaking. Next, the gel was prehybridized in Church's buffer (1% bovine serum albumin [BSA], 1 mM EDTA, 0.5 M $NaPo_4$ at pH 7.2, 7% SDS) for 1 h at 55°C before adding a ^{32}P-end-labeled $(CCCTAA)_3$ telomeric probe. The gel was washed three times for 30 min in 4× SSC at 50°C and once for 30 min in 4× SSC + 0.1% SDS at 25°C and then exposed on a phosphorimager screen.

Conditional CTC1 loop-out

Conditional CTC1 cell lines were generated in WIBR3 hESCs (National Institutes of Health stem cell registry 0079). Exon 5 deletion (Supplemental Fig. S8A, step 1) was generated via electroporation of CTC1 guide RNAs 1 and 2, which were cloned into a pX330 vector backbone. Cells were clonally isolated and genotyped to identify heterozygous $CTC1^{\Delta/+}$ clones. The repair template, consisting of a LoxP-flanked exon 5 alongside an FRT-flanked PGK-PURO cassette, was inserted (Supplemental Fig. S8A, step 2) by electroporation of CTC1 guide 3, which targeted the junction on the Δ allele. After puromycin selection and clonal genotyping of successful $CTC1^{\Delta Puro/+}$ clones, the PGK-PURO cassette was removed (Supplemental Fig. S8A, step 3) via transfection with Flp mRNA to generate $CTC1^{F/+}$ cells. Next, the remaining wild-type allele was removed (Supplemental Fig. S8A, step 4) by retargeting cells with CTC1 guide 1 and guide 2, generating $CTC1^{F/-}$ cells. A CAGGS-ERT2-Cre-ERT2 expression cassette was then integrated at the *AAVS1* locus in both $CTC1^{F/+}$ and $CTC1^{F/-}$ cells. To loop out the conditional CTC1 allele, cells were treated with 2 µM 4-hydroxytamoxifen for 48 h.

CTC1 and SHLD1 targeting in POT1 FS and Syn cells

POT1 frameshift and synonymous cells under ATRi were targeted with two sgRNAs targeting exon 5 of CTC1 or one sgRNA targeting exon 1 of SHLD1. Nucleofection and clonal isolation were performed as described in the respective sections above. On day 19 after nucleofection, the CTC1 targeted plates duplicated on day 12 were fixed and stained with hNA and DAPI as outlined above in "TIF Staining." Cells were imaged and analyzed with a Celigo imager. A bulk-nucleofected population was kept in culture concurrent with the clonal plates and then seeded at one, three, and 10 cells/well 14 days after nucleofection to clonally isolate cells at a later time point. These later time point clones were lysed and genotyped 26 days after nucleofection.

Competing interest statement

The authors declare no competing interests

Acknowledgments

We dedicate this work to our friend and colleague John Boyle (who passed away on August 9, 2024), in honor of his personal and professional battle against cancer and his scientific contribution to this study. D.H. is supported by Research Scholar Grants from the American Cancer Society (133396-RSG-19-029-01-DMC). The work in the Hockemeyer laboratory was supported by the Siebel Stem Cell Institute, National Institutes of Health (NIH; R01-HL131744). J.S. is supported by the California Institute for Regenerative Medicine training program (EDUC4-12790). G.E.G. is supported by a Jane Coffin Childs Postdoctoral Fellowship. The research in H.L.'s laboratory was supported by the CRISPR Cures for Cancer Initiative. The research in Y.S.S.'s laboratory was supported in part by an NIH grant (R35-GM134922). The AAVS1 targeting construct to express the CRE-ER was a generous gift from Frank Soldner, Albert Einstein Institute of Medicine.

Author contributions: A.M., J.S., R.B.-C., H.L., and D.H. designed the experiments with the advice of Y.S.S. Experiments were performed by J.S., R.B.-C., H.L., and D.H. with the help of S.T., R.L., R.H., and A.P. The TIF linear regression model was developed by J.G. and H.L. with the advice of Y.S.S. and M.J. The conditional CTC1 KO hESCs were generated by S.J. and J.B. The data were analyzed by A.M., J.S., H.L., and D.H. Structural analysis and visualization were performed by G.E.G. A.M., J.S., H.L., and D.H. wrote the manuscript.

References

Aramburu T, Kelich J, Rice C, Skordalakes E. 2022. POT1–TPP1 binding stabilizes POT1, promoting efficient telomere maintenance. *Comput Struct Biotechnol J* **20:** 675–684. doi:10.1016/j.csbj.2022.01.005

Bainbridge MN, Armstrong GN, Gramatges MM, Bertuch AA, Jhangiani SN, Doddapaneni H, Lewis L, Tombrello J, Tsavachidis S, Liu Y, et al. 2015. Germline mutations in shelterin complex genes are associated with familial glioma. *J Natl Cancer Inst* **107:** dju384. doi:10.1093/jnci/dju384

Boersma V, Moatti N, Segura-Bayona S, Peuscher MH, van der Torre J, Wevers BA, Orthwein A, Durocher D, Jacobs JJL. 2015. MAD2L2 controls DNA repair at telomeres and DNA breaks by inhibiting 5′ end resection. *Nature* **521:** 537–540. doi:10.1038/nature14216

Buisson R, Niraj J, Rodrigue A, Ho CK, Kreuzer J, Foo TK, Hardy EJ-L, Dellaire G, Haas W, Xia B, et al. 2017. Coupling of homologous recombination and the checkpoint by ATR. *Mol Cell* **65:** 336–346. doi:10.1016/j.molcel.2016.12.007

Cai SW, Takai H, Zaug AJ, Dilgen TC, Cech TR, Walz T, de Lange T. 2024. POT1 recruits and regulates CST–Polα/primase at human telomeres. *Cell* **187:** 3638–3651.e18. doi:10.1016/j.cell.2024.05.002

Calvete O, Martinez P, Garcia-Pavia P, Benitez-Buelga C, Paumard-Hernández B, Fernandez V, Dominguez F, Salas C, Romero-Laorden N, Garcia-Donas J, et al. 2015. A mutation in the POT1 gene is responsible for cardiac angiosarcoma in TP53-negative Li-Fraumeni-like families. *Nat Commun* **6:** 8383. doi:10.1038/ncomms9383

Calvete O, Garcia-Pavia P, Domínguez F, Bougeard G, Kunze K, Braeuninger A, Teule A, Lasa A, Ramón y Cajal T, Llort G, et al. 2017. The wide spectrum of POT1 gene variants correlates with multiple cancer types. *Eur J Hum Genet* **25:** 1278–1281. doi:10.1038/ejhg.2017.134

Chen C, Gu P, Wu J, Chen X, Niu S, Sun H, Wu L, Li N, Peng J, Shi S, et al. 2017. Structural insights into POT1–TPP1 interaction and POT1 C-terminal mutations in human cancer. *Nat Commun* **8:** 14929. doi:10.1038/ncomms14929

Chubb D, Broderick P, Dobbins SE, Frampton M, Kinnersley B, Penegar S, Price A, Ma YP, Sherborne AL, Palles C, et al. 2016. Rare disruptive mutations and their contribution to the heritable risk of colorectal cancer. *Nat Commun* **7:** 11883. doi:10.1038/ncomms11883

Clement K, Rees H, Canver MC, Gehrke JM, Farouni R, Hsu JY, Cole MA, Liu DR, Joung JK, Bauer DE, et al. 2019. CRISPResso2 provides accurate and rapid genome editing sequence analysis. *Nat Biotechnol* **37:** 224–226. doi:10.1038/s41587-019-0032-3

DeBoy EA, Tassia MG, Schratz KE, Yan SM, Cosner ZL, McNally EJ, Gable DL, Xiang Z, Lombard DB, Antonarakis ES, et al. 2023. Familial clonal hematopoiesis in a long telomere syndrome. *N Engl J Med* **388:** 2422–2433. doi:10.1056/NEJMoa2300503

de Lange T. 2018. Shelterin-mediated telomere protection. *Annu Rev Genet* **52:** 223–247. doi:10.1146/annurev-genet-032918-021921

Denchi EL, de Lange T. 2007. Protection of telomeres through independent control of ATM and ATR by TRF2 and POT1. *Nature* **448:** 1068–1071. doi:10.1038/nature06065

Drozdetskiy A, Cole C, Procter J, Barton GJ. 2015. JPred4: a protein secondary structure prediction server. *Nucleic Acids Res* **43:** W389–W394. doi:10.1093/nar/gkv332

Evans R, O'Neill M, Pritzel A, Antropova N, Senior A, Green T, Žídek A, Bates R, Blackwell S, Yim J, et al. 2022. Protein complex prediction with AlphaFold-Multimer. bioRxiv doi:10.1101/2021.10.04.463034

Feng X, Hsu S-J, Kasbek C, Chaiken M, Price CM. 2017. CTC1-mediated C-strand fill-in is an essential step in telomere length maintenance. *Nucleic Acids Res* **45:** 4281–4293. doi:10.1093/nar/gkx125

Ghanim GE, Fountain AJ, van Roon A-MM, Rangan R, Das R, Collins K, Nguyen THD. 2021. Structure of human telomerase holoenzyme with bound telomeric DNA. *Nature* **593:** 449–453. doi:10.1038/s41586-021-03415-4

Glousker G, Briod A-S, Quadroni M, Lingner J. 2020. Human shelterin protein POT1 prevents severe telomere instability induced by homology-directed DNA repair. *EMBO J* **39:** e104500. doi:10.15252/embj.2020104500

Goddard TD, Huang CC, Meng EC, Pettersen EF, Couch GS, Morris JH, Ferrin TE. 2018. UCSF ChimeraX: meeting modern challenges in visualization and analysis. *Protein Sci* **27:** 14–25. doi:10.1002/pro.3235

Goldstein AM, Qin R, Chu EY, Elder DE, Massi D, Adams DJ, Harms PW, Robles-Espinoza CD, Newton-Bishop JA, Bishop DT, et al. 2023. Association of germline variants in telomere maintenance genes (POT1, TERF2IP, ACD, and TERT) with spitzoid morphology in familial melanoma: a multi-center case series. *JAAD Int* **11:** 43–51. doi:10.1016/j.jdin.2023.01.013

Gu P, Wang Y, Bisht KK, Wu L, Kukova L, Smith EM, Xiao Y, Bailey S, Lei M, Nandakumar J, et al. 2017. Human Pot1 OB-fold mutations unleash rampant telomere instability to initiate tumorigenesis. *Oncogene* **36:** 1939–1951. doi:10.1038/onc.2016.405

Gupta R, Somyajit K, Narita T, Maskey E, Stanlie A, Kremer M, Typas D, Lammers M, Mailand N, Nussenzweig A, et al. 2018. DNA repair network analysis reveals shieldin as a key regulator of NHEJ and PARP inhibitor sensitivity. *Cell* **173:** 972–988.e23. doi:10.1016/j.cell.2018.03.050

Haeussler M, Schönig K, Eckert H, Eschstruth A, Mianné J, Renaud J-B, Schneider-Maunoury S, Shkumatava A, Teboul L, Kent J, et al. 2016. Evaluation of off-target and on-target scoring algorithms and integration into the guide RNA selection tool CRISPOR. *Genome Biol* **17:** 148. doi:10.1186/s13059-016-1012-2

Hemann MT, Strong MA, Hao LY, Greider CW. 2001. The shortest telomere, not average telomere length, is critical for cell viability and chromosome stability. *Cell* **107:** 67–77. doi:10.1016/S0092-8674(01)00504-9

Hockemeyer D, Sfeir AJ, Shay JW, Wright WE, de Lange T. 2005. POT1 protects telomeres from a transient DNA damage response and determines how human chromosomes end. *EMBO J* **24:** 2667–2678. doi:10.1038/sj.emboj.7600733

Hockemeyer D, Daniels J-P, Takai H, de Lange T. 2006. Recent expansion of the telomeric complex in rodents: two distinct POT1 proteins protect mouse telomeres. *Cell* **126:** 63–77. doi:10.1016/j.cell.2006.04.044

Hsu PD, Scott DA, Weinstein JA, Ran FA, Konermann S, Agarwala V, Li Y, Fine EJ, Wu X, Shalem O, et al. 2013. DNA targeting specificity of RNA-guided Cas9 nucleases. *Nat Biotechnol* **31:** 827–832. doi:10.1038/nbt.2647

Huang H, Hu C, Na J, Hart SN, Gnanaolivu RD, Abozaid M, Rao T, Tecleab YA, Pesaran T, Lyra PCM, et al. 2025. Functional evaluation and clinical classification of BRCA2 variants. *Nature* **638:** 528–537. doi:10.1038/s41586-024-08388-8

Jumper J, Evans R, Pritzel A, Green T, Figurnov M, Ronneberger O, Tunyasuvunakool K, Bates R, Žídek A, Potapenko A, et al. 2021. Highly accurate protein structure prediction with AlphaFold. *Nature* **596:** 583–589. doi:10.1038/s41586-021-03819-2

Kelich J, Aramburu T, van der Vis JJ, Showe L, Kossenkov A, van der Smagt J, Massink M, Schoemaker A, Hennekam E, Veltkamp M, et al. 2022. Telomere dysfunction implicates POT1 in patients with idiopathic pulmonary fibrosis. *J Exp Med* **219:** e20211681. doi:10.1084/jem.20211681

Kim D, Liu Y, Oberly S, Freire R, Smolka MB. 2018. ATR-mediated proteome remodeling is a major determinant of homologous recombination capacity in cancer cells. *Nucleic Acids Res* **46:** 8311–8325. doi:10.1093/nar/gky625

Kim W, Hennick K, Johnson J, Finnerty B, Choo S, Short SB, Drubin C, Forster R, McMaster ML, Hockemeyer D. 2021. Cancer-associated POT1 mutations lead to telomere elongation without induction of a DNA damage response. *EMBO J* **40:** e107346. doi:10.15252/embj.2020107346

Laprade H, Querido E, Smith MJ, Guérit D, Crimmins H, Conomos D, Pourret E, Chartrand P, Sfeir A. 2020. Single-molecule imaging of telomerase RNA reveals a recruitment-retention model for telomere elongation. *Mol Cell* **79:** 115–126.e6. doi:10.1016/j.molcel.2020.05.005

Latrick CM, Cech TR. 2010. POT1–TPP1 enhances telomerase processivity by slowing primer dissociation and aiding translocation. *EMBO J* **29:** 924–933. doi:10.1038/emboj.2009.409

Lee SS, Bohrson C, Pike AM, Wheelan SJ, Greider CW. 2015. ATM kinase is required for telomere elongation in mouse and human cells. *Cell Rep* **13:** 1623–1632. doi:10.1016/j.celrep.2015.10.035

Lei M, Podell ER, Cech TR. 2004. Structure of human POT1 bound to telomeric single-stranded DNA provides a model

for chromosome end-protection. *Nat Struct Mol Biol* **11:** 1223–1229. doi:10.1038/nsmb867

Lengner CJ, Gimelbrant AA, Erwin JA, Cheng AW, Guenther MG, Welstead GG, Alagappan R, Frampton GM, Xu P, Muffat J, et al. 2010. Derivation of pre-X inactivation human embryonic stem cells under physiological oxygen concentrations. *Cell* **141:** 872–883. doi:10.1016/j.cell.2010.04.010

Li Y, Xie Y, Wang D, Xu H, Ye J, Yin JC, Chen J, Yan J, Ye B, Chen C. 2022. Whole exome sequencing identified a novel POT1 variant as a candidate pathogenic allele underlying a Li-Fraumeni-like family. *Front Oncol* **12:** 963364. doi:10.3389/fonc.2022.963364

Li H, Bartke R, Zhao L, Verma Y, Horacek A, Rechav Ben-Natan A, Pangilinan GR, Krishnappa N, Nielsen R, Hockemeyer D. 2024. Functional annotation of variants of the BRCA2 gene via locally haploid human pluripotent stem cells. *Nat Biomed Eng* **8:** 165–176. doi:10.1038/s41551-023-01065-7

Loayza D, Parsons H, Donigian J, Hoke K, de Lange T. 2004. DNA binding features of human POT1. *J Biol Chem* **279:** 13241–13248. doi:10.1074/jbc.M312309200

McMaster ML, Sun C, Landi MT, Savage SA, Rotunno M, Yang XR, Jones K, Vogt A, Hutchinson A, Zhu B, et al. 2018. Germline mutations in protection of telomeres 1 in two families with Hodgkin lymphoma. *Br J Haematol* **181:** 372–377. doi:10.1111/bjh.15203

Mirdita M, Steinegger M, Söding J. 2019. MMseqs2 desktop and local web server app for fast, interactive sequence searches. *Bioinformatics* **35:** 2856–2858. doi:10.1093/bioinformatics/bty1057

Mirdita M, Schütze K, Moriwaki Y, Heo L, Ovchinnikov S, Steinegger M. 2022. Colabfold: making protein folding accessible to all. *Nat Methods* **19:** 679–682. doi:10.1038/s41592-022-01488-1

Mirman Z, Lottersberger F, Takai H, Kibe T, Gong Y, Takai K, Bianchi A, Zimmermann M, Durocher D, de Lange T. 2018. 53BP1–RIF1–shieldin counteracts DSB resection through CST- and Polα-dependent fill-in. *Nature* **560:** 112–116. doi:10.1038/s41586-018-0324-7

Mirman Z, Sasi NK, King A, Chapman JR, de Lange T. 2022. 53BP1/shieldin-dependent DSB processing in BRCA1-deficient cells requires CST/Polα/primase fill-in synthesis. *Nat Cell Biol* **24:** 51–61. doi:10.1038/s41556-021-00812-9

Noordermeer SM, Adam S, Setiaputra D, Barazas M, Pettitt SJ, Ling AK, Olivieri M, Álvarez-Quilón A, Moatti N, Zimmermann M, et al. 2018. The shieldin complex mediates 53BP1-dependent DNA repair. *Nature* **560:** 117–121. doi:10.1038/s41586-018-0340-7

Palm W, Hockemeyer D, Kibe T, de Lange T. 2009. Functional dissection of human and mouse POT1 proteins. *Mol Cell Biol* **29:** 471–482. doi:10.1128/MCB.01352-08

Ramsay AJ, Quesada V, Foronda M, Conde L, Martínez-Trillos A, Villamor N, Rodríguez D, Kwarciak A, Garabaya C, Gallardo M, et al. 2013. POT1 mutations cause telomere dysfunction in chronic lymphocytic leukemia. *Nat Genet* **45:** 526–530. doi:10.1038/ng.2584

Rice C, Shastrula PK, Kossenkov AV, Hills R, Baird DM, Showe LC, Doukov T, Janicki S, Skordalakes E. 2017. Structural and functional analysis of the human POT1–TPP1 telomeric complex. *Nat Commun* **8:** 14928. doi:10.1038/ncomms14928

Robles-Espinoza CD, Harland M, Ramsay AJ, Aoude LG, Quesada V, Ding Z, Pooley KA, Pritchard AL, Tiffen JC, Petljak M, et al. 2014. POT1 loss-of-function variants predispose to familial melanoma. *Nat Genet* **46:** 478–481. doi:10.1038/ng.2947

Sahu S, Galloux M, Southon E, Caylor D, Sullivan T, Arnaudi M, Zanti M, Geh J, Chari R, Michailidou K, et al. 2025. Saturation genome editing-based clinical classification of BRCA2 variants. *Nature* **638:** 538–545. doi:10.1038/s41586-024-08349-1

Sekne Z, Ghanim GE, van Roon A-MM, Nguyen THD. 2022. Structural basis of human telomerase recruitment by TPP1–POT1. *Science* **375:** 1173–1176. doi:10.1126/science.abn6840

Shen E, Xiu J, López GY, Bentley R, Jalali A, Heimberger AB, Bainbridge MN, Bondy ML, Walsh KM. 2020. *POT1* mutation spectrum in tumor types commonly diagnosed among *POT1*-associated hereditary cancer syndrome families. *J Med Genet* **57:** 664–670. doi:10.1136/jmedgenet-2019-106657

Shi J, Yang XR, Ballew B, Rotunno M, Calista D, Fargnoli MC, Ghiorzo P, Bressac-de Paillerets B, Nagore E, Avril MF, et al. 2014. Rare missense variants in POT1 predispose to familial cutaneous malignant melanoma. *Nat Genet* **46:** 482–486. doi:10.1038/ng.2941

Speedy HE, Kinnersley B, Chubb D, Broderick P, Law PJ, Litchfield K, Jayne S, Dyer MJS, Dearden C, Follows GA, et al. 2016. Germ line mutations in shelterin complex genes are associated with familial chronic lymphocytic leukemia. *Blood* **128:** 2319–2326. doi:10.1182/blood-2016-01-695692

Takai H, Smogorzewska A, de Lange T. 2003. DNA damage foci at dysfunctional telomeres. *Curr Biol* **13:** 1549–1556. doi:10.1016/S0960-9822(03)00542-6

Takai H, Jenkinson E, Kabir S, Babul-Hirji R, Najm-Tehrani N, Chitayat DA, Crow YJ, de Lange T. 2016. A POT1 mutation implicates defective telomere end fill-in and telomere truncations in coats plus. *Genes Dev* **30:** 812–826. doi:10.1101/gad.276873.115

Takai H, Aria V, Borges P, Yeeles JTP, de Lange T. 2024. CST–polymerase α-primase solves a second telomere end-replication problem. *Nature* **627:** 664–670. doi:10.1038/s41586-024-07137-1

Teixeira MT, Arneric M, Sperisen P, Lingner J. 2004. Telomere length homeostasis is achieved via a switch between telomerase-extendible and -nonextendible states. *Cell* **117:** 323–335. doi:10.1016/S0092-8674(04)00334-4

Tesmer VM, Brenner KA, Nandakumar J. 2023. Human POT1 protects the telomeric ds–ss DNA junction by capping the 5′ end of the chromosome. *Science* **381:** 771–778. doi:10.1126/science.adi2436

Tong AS, Stern JL, Sfeir A, Kartawinata M, de Lange T, Zhu X-D, Bryan TM. 2015. ATM and ATR signaling regulate the recruitment of human telomerase to telomeres. *Cell Rep* **13:** 1633–1646. doi:10.1016/j.celrep.2015.10.041

Wang F, Podell ER, Zaug AJ, Yang Y, Baciu P, Cech TR, Lei M. 2007. The POT1–TPP1 telomere complex is a telomerase processivity factor. *Nature* **445:** 506–510. doi:10.1038/nature05454

Wang H, Ma T, Zhang X, Chen W, Lan Y, Kuang G, Hsu S-J, He Z, Chen Y, Stewart J, et al. 2023. CTC1 OB-B interaction with TPP1 terminates telomerase and prevents telomere overextension. *Nucleic Acids Res* **51:** 4914–4928. doi:10.1093/nar/gkad237

Wilson TLS, Hattangady N, Lerario AM, Williams C, Koeppe E, Quinonez S, Osborne J, Cha KB, Else T. 2017. A new POT1 germline mutation—expanding the spectrum of POT1-associated cancers. *Fam Cancer* **16:** 561–566. doi:10.1007/s10689-017-9984-y

Wu Y, Poulos RC, Reddel RR. 2020. Role of POT1 in human cancer. *Cancers (Basel)* **12:** 2739. doi:10.3390/cancers12102739

Xin H, Liu D, Wan M, Safari A, Kim H, Sun W, O'Connor MS, Songyang Z. 2007. TPP1 is a homologue of ciliate TEBP-β and interacts with POT1 to recruit telomerase. *Nature* **445:** 559–562. doi:10.1038/nature05469

Xu G, Chapman JR, Brandsma I, Yuan J, Mistrik M, Bouwman P, Bartkova J, Gogola E, Warmerdam D, Barazas M, et al. 2015. REV7 counteracts DNA double-strand break resection and affects PARP inhibition. *Nature* **521:** 541–544. doi:10.1038/nature14328

Ye JZ-S, Hockemeyer D, Krutchinsky AN, Loayza D, Hooper SM, Chait BT, de Lange T. 2004. POT1-interacting protein PIP1: a telomere length regulator that recruits POT1 to the TIN2/TRF1 complex. *Genes Dev* **18:** 1649–1654. doi:10.1101/gad.1215404